JOURNAL OF PROPULSION AND POWER
Vol. 16, No. 3, May–June 2000

Measurements of Ions from High-Current Hollow Cathodes Using Electrostatic Energy Analyzer

Ikuya Kameyama* and Paul J. Wilbur†
Colorado State University, Fort Collins, Colorado 80523

Energy distributions of ions emanating from high-current, xenon hollow cathodes were measured using an electrostatic energy analyzer. Ions with energies much greater than maximum potential differences between electrodes were observed. This result is consistent with previous retarding-potential-analyzer data, but the electrostatic-energy-analyzer data show much more complicated structures. To characterize these distributions, they were fit with simple Gaussian functions, and the effects of discharge conditions on high-energy-ion characteristics were investigated. The energy of ions emanating from cathodes appears to increase as discharge current is increased or cathode flow rate is reduced. Higher discharge currents cause the ion populations in the high-energy tails of the distributions to increase in the plume mode while the high-energy tails decrease in the spot mode.

Nomenclature

A = effective electrostatic energy analyzer (ESA) acceptance area
e = electron charge
$g(\varepsilon)$ = energy-distribution function
$g'(\varepsilon)$ = approximated Gaussian component of energy-distribution function
J_d = discharge current
J_k = keeper current
$J(\varepsilon)$ = collector ion current
m = xenon ion mass
$\dot{m}$ = xenon flow rate
n = ion population in the Gaussian component
P_0 = ambient pressure
V_d = anode potential
V_k = keeper potential
ε = ion energy
ε_0 = mean energy of the Gaussian component
$\tilde{\varepsilon}$ = energy-resolution width of the ESA
σ = energy dispersion associated with the Gaussian component

Introduction

LONG-DURATION operation of the electron source at high-current conditions is generally considered to be required for high-power ion propulsion systems,[1–4] and hollow cathodes appear to be suitable for these applications. For example, operation of 5- and 10-kW ion thrusters with xenon propellant has been initiated, and a life test has been conducted for a thruster system in which two hollow cathodes were used to provide electrons.[5] In this test the discharge-chamber hollow cathode supplied a ~22-A electron current, and the neutralizer cathode supplied a ~6-A electron current for more than 500 h. For both cathodes severe sputter erosion was observed on surfaces located downstream of them. Another xenon-hollow-cathode life test was conducted to demonstrate more than 5000 h of operation at a 25-A discharge current, and the test ended with severe sputter damage to both a starter electrode installed close to the cathode and its support.[6]

Received 14 July 1995; revision received 17 May 1999; accepted for publication 8 July 1999.

*Research Assistant, Department of Mechanical Engineering; currently Research and Development Engineer, Ion Tech, Inc., 2330 E. Prospect, Fort Collins, Colorado 80525. Member AIAA.

†Professor, Department of Mechanical Engineering. Senior Member AIAA.

An intensive investigation of erosion phenomena conducted by Friedly and Wilbur has suggested that high-energy ion jets, which could cause a severe sputter erosion on components downstream, emanate from high-current hollow cathodes.[7] This work was accomplished using a retarding potential analyzer (RPA) as a charged-particle detector and erosion badges placed downstream of the cathode to sense erosion rates. On the basis of measurements made at different badge locations, it was postulated that the jets emanate from a point near the cathode orifice. Also from ion-energy profiles obtained using the RPA, the suggestion was made that the ion current density, the average ion-energy, and ion-energy spread all increase as the discharge current is increased. Another measurement of energy distributions associated with ions produced by high-current, xenon hollow cathodes was conducted by Latham et al.[8] This investigation was also conducted using an RPA to measure the ion-energy distribution. Again, jets of ions with energies greater than the potential differences between electrodes were observed.

In this paper other test results showing energy distributions associated with ions emitted from high-current hollow cathodes are presented. The cathodes are operated on xenon propellant and ion energies are measured using an electrostatic energy analyzer (ESA). The effects of changes in cathode orifice shape, discharge current, and flow rate on the ion-energy distribution functions are examined.

Apparatus and Procedures

The basic schematic diagram associated with the hollow-cathode tests reported in this article is shown in Fig. 1. A cylindrical anode was provided to sustain the discharge. To initiate and stabilize the discharge, a keeper was positioned in front of the cathode. This configuration was chosen to simulate typical, hollow-cathode operation within typical main discharge chambers of ion-propulsion systems.

The cathode was connected to the plenum shown in Fig. 1, and the interior pressure of the plenum was monitored using a capacitance pressure gauge. The water-cooled anode was a 1.8-mm-thick copper plate that had been rolled into 60-mm inner-diam × 115-mm-long hollow cylinder. As shown in Fig. 1, it extended 75 mm downstream of the orifice plate. It had an approximately 35-mm-wide slit on one side through which the cathode discharge could be observed. The keeper electrode was constructed from a 1.5-mm-diam tantalum wire that was bent into a 4.0-mm-inner-diam toroidal ring, and it was positioned 1.0 mm downstream of the cathode orifice.

The orificed hollow cathodes used in this study were constructed from 6.4-mm-diam tantalum tubes with 1.6-mm-thick thoriated-tungsten orifice plates electron-beam-welded on one end. The dimensions of the orifice bores were measured before and after each experiment to determine if they had enlarged during a test. Bore

Table 1 Hollow cathode orifices

Minimum orifice diameter (upstream), mm	Maximum orifice diameter (downstream), mm	Designation in text
0.71	0.71	straight
0.71	1.65	16-deg-chamfered[a]

[a]Chamfers were introduced as a result of cathode operation at high current, and angles are approximated based on the assumption of straight side walls.

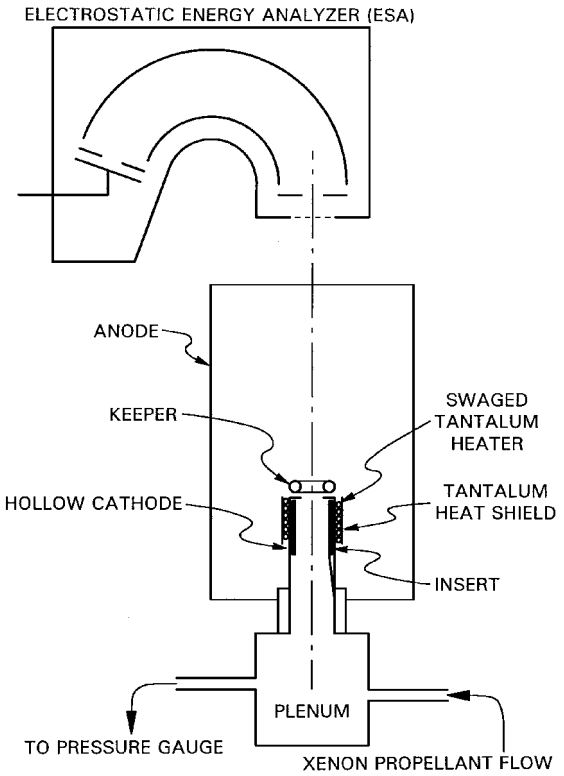

Fig. 1 Schematic diagram of experimental facility.

enlargement was not observed at the upstream end of the orifices. It appeared that enlargement, which was reflected in plenum pressure decrease, occurred only at high discharge currents (>20 ~ 30 A). Modest enlargement could have occurred at lower discharge currents. However, they induced no major changes in measured ion-energy distributions. The dimensions of cathode orifices used in these experiments and their designations based on measured downstream diameters are given in Table 1. Each cathode contained an insert positioned as shown in Fig. 1. The inserts (low-work-function electron emitters) were made by rolling a six-layer wrap of 0.013-mm-thick tantalum foil around a 4-mm diam × 20-mm-long tube. This wrap was spot-welded to a 3-mm-wide, 45-mm-long, 0.25-mm-thick tantalum ribbon, and the ribbon was in turn spot-welded to the inner surface of the cathode tube after the wrap had been dipped in a solution containing barium and strontium carbonates (Chemical R-500). Sintered tungsten inserts, which are generally used in flight-qualified hollow cathodes, were not investigated because previous research had shown that insert type did not affect ion-energy distributions significantly.[9] A swaged tantalum heater 15 mm in length was friction-bonded to the cathode tube, and 0.013-mm-thick tantalum foil heat shields were also used to reduce the radiation heat loss from it.

The ESA[10] used in this study as a probe to detect ions emitted from the hollow cathode is shown schematically in Fig. 2. This unit (Comstock Inc., Model AC-901) operates by establishing a radial, electrostatic field between two copper surfaces, which form segments of spheres having a common center and different radii. Charged particles that pass through the entrance collimator are focused along different paths depending upon their kinetic

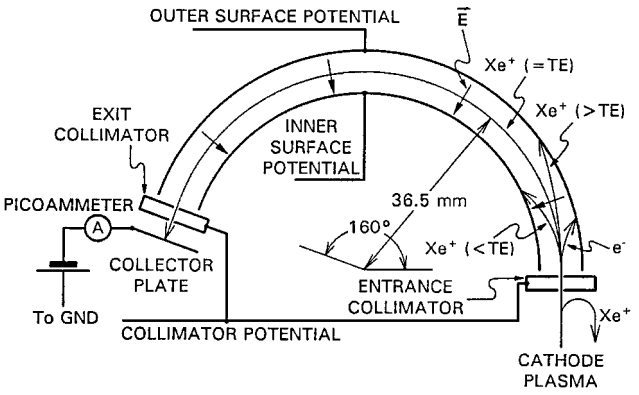

Fig. 2 Schematic diagram of ESA.

energy, charge, and mass. The electrostatic fields within the unit were established by setting potential differences between the inner and outer surfaces and the collimator sets. Under this condition only those ions with a prescribed kinetic energy [the transmission energy (TE)] at the entrance collimator are able to pass through the unit with a specific curvature of trajectories (36.5 mm as shown in Fig. 2). As suggested in Fig. 2, ions with greater and lesser energies will strike the outer and inner surfaces, respectively. To sense the ion-energy distribution, potentials on the inner, outer, and collimator surfaces are swept together with respect to facility ground potential, thereby changing the amount of acceleration or deceleration experienced by ions as they approach the entrance collimator from the cathode-plasma plume. Entrance- and exit-collimator sets had 2.0-mm-diam apertures spaced 7.8 mm apart.

To prevent transient discharges between the cathode plasma and facility ground, the hollow-cathode/anode assembly was floated. The cathode-to-ground potential difference, which was almost constant during each test and typically 0 ~ 5 V, was monitored during the tests, so that the energies at which ions would strike a cathode potential surface would be known. Ions were collected on the stainless-steel plate shown downstream of the exit collimator in Fig. 2, and the currents were sensed by a picoammeter that retransmitted this signal along with the collimator potential measured with respect to ground to an X-Y recorder. The collector plate was biased about 30 V negative with respect to the ground potential by batteries to eliminate any ion dispersion that could have been induced by space charge effects. In addition, an electromesh nickel screen with 85%-optical-transparency and square openings, 0.24 mm on a side, was placed on the upstream side of a 6.4-mm-diam entrance aperture on a grounded aluminum box that enclosed the entire ESA. It provided a potential barrier, which limited electron flow into the device and, therefore, the resultant collection of stray currents on electrical connection points and active surfaces. A 1.8-mm-thick soft iron box, which provided shielding against geomagnetic-field effects, also enclosed the ESA. The ion currents were measured using a 10-eV ESA transmission energy, which was established via internal bias conditions, and the absolute bias on the instrument was varied over the range that yielded ion energies from a few to 100 eV.

As shown in Fig. 1, the ESA was positioned 180 mm downstream of the cathode orifice with its entrance-collimator axis aligned with the cathode axis (i.e., looking at the cathode orifice) for all of the experiments described herein. This configuration was used because it was anticipated that the energetic ions would be created near the orifice. To confirm this, a series of ESA measurements were made with the probe positioned the same vertical distance from the cathode but moved, so that it was 1) on centerline pointing at the orifice, 2) ~1 cm off centerline with its entrance axis parallel to the cathode axis, 3) off centerline and pointing toward the cathode orifice, and 4) off centerline pointed away from the orifice. In cases 1, 2, and 3 the acceptance angle of the ESA was such that some ions created at the orifice or in a plume immediately downstream

of it would be collected. In case 4 the orientation was such that none of these ions should have been collected. These experiments demonstrated that 1) the distribution of energies among the ions was similar whenever the ESA was pointed at the orifice, 2) there were dramatic reductions in the currents of high energy detected by the probe when it was not pointed at the cathode orifice, and 3) almost no ion currents were detected when the ESA was pointed far away from the cathode orifice.

The experiments were initiated by evacuating the vacuum chamber below 2.0×10^{-6} Torr (2.7×10^{-4} Pa) using a cryopump. The cathode was heated using a heater current of 5 A for 15 min while xenon was being bled through the cathode at about 0.3 sccm [standard cubic centimeters per min] of Xe (i.e., at 20 mA eq. Xe) to flush out possible contaminants. After an additional 15 min of heating at a heater current of 8 A with zero xenon flow, the keeper was biased to 160 V with respect to the cathode, and the xenon flow rate was increased slowly until a discharge was initiated between the cathode and keeper. After the keeper discharge had stabilized at 0.5 A and ~20 V, anode power was applied. Before ion-current data sensed by the ESA were collected, operating parameters such as xenon flow rate $\dot{m}$, keeper current J_k, and discharge current J_d were set at the desired conditions, and the discharge was allowed to stabilize for at least 30 min. During the experiments, the ambient pressure P_0 was maintained in the order of 10^{-4} Torr (10^{-2} Pa), as indicated in the associated figures.

Results

Discharge Current Effects

Figure 3 shows the anode and keeper potentials (V_d and V_k, respectively), measured as functions of discharge current for the cathode-orifice configurations. Note that the keeper current was fixed at 0.5 A, and, therefore, the total emission current from the hollow cathode was 0.5 A greater than the discharge current. As Fig. 3 suggests, the anode and the cathode potentials did not change suddenly with discharge current except in the case where the straight-orifice cathode was used. In this case a sudden drop was observed as the current was increased from 5 to 7 A. This change was observed at the same point where the transition from the plume mode to the spot mode occurred as described in previous research.[11–13] Keeper and anode potentials were always less than 20 V. Because plasma potentials are generally near the potential of the most positive electrode in contact with the plasmas (the anode, in this case) and the energy distributions were measured with respect to the cathode potential, one might expect that the maximum potential difference through which ions could be accelerated would be that between the anode and the cathode. Thus the maximum ion energies would be less than 20 eV for operation under all of the discharge current conditions indicated in Fig. 3.

The typical trend observed in the ESA collector current as discharge current is increased is shown in Fig. 4. These particular data

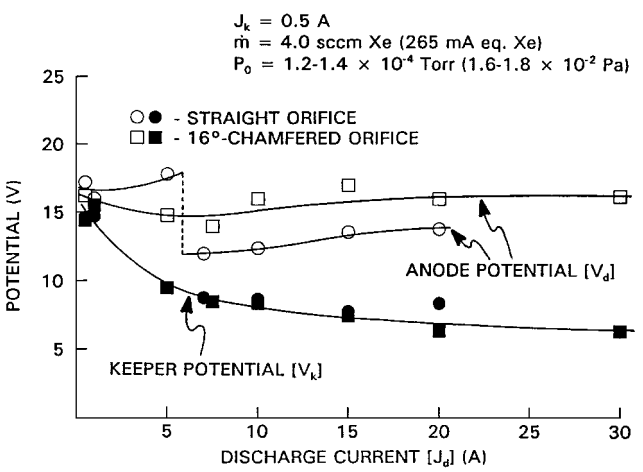

Fig. 3 Effects of discharge current on anode and keeper potentials.

obtained using the 16-deg-chamfered orifice generally show four peaks that reflect the presence of four distinct groups of ions at modest discharge currents (5 ~ 10 A). As discharge current was changed, these four groups of ions appeared to change their energies and ion populations so that their relative prominences, therefore, also changed. The highest peaks that are particularly apparent in the $J_d = 0.5$- and 1.0-A plots pertain to the cathode-to-anode potential differences and they correspond to ions produced in the downstream (ambient) plasma that acquire these kinetic energies as they are accelerated to the reference (cathode) potential. The sharp peaks at lesser energies in some of these plots appear to reflect ions produced close to the ESA possibly by charge exchange between ions and neutral atoms, and they do not appear to be representative of ions in the ambient plasma. The latter group of ions is of no significant interest compared with higher-energy groups that are especially apparent at higher discharge currents because the higher-energy groups induce much more rapid erosion of cathode-potential thruster surfaces.[14] Hence, the remainder of this article will focus primarily on these higher energy groups.

Of particular interest is the fact that the tails of the high-energy groups extend far beyond the values that could be induced by accelerating ions from the most positive electrode (the anode) to the most negative electrode (the cathode). As discharge current is increased, the plots of Fig. 4 show that the low-energy peaks become less significant while the populations associated with the high-energy tails increase. Generally, energies of these high-energy tails were observed to increase almost continuously with discharge current. In fact, above a 15-A discharge current the low-energy peaks were generally obscured. This could be caused by a high ambient-plasma density, which would be expected to reduce the signal-to-noise ratio at low energies. It also could be caused by greater temperatures of the ambient plasma, which were observed at higher discharge currents by Friedly and Wilbur[7] and would generally be expected to cause the peak to broaden as the high-energy one does in the various plots of Fig. 4.

To track the behavior of each peak associated with the plots of Fig. 4, Gaussian components were computed, and the Gaussian parameters associated with each peak were then plotted as a function of discharge current. First, a raw-data plot of the ESA collector current is converted to ion energy distributions. Because the ESA eliminates a large fraction of the ions with off-axial velocity components in the entrance collimator and electrostatic field sections, it would show energy distributions of ions that have velocity directions within a narrow range, whereas typical energy distribution functions are defined for ions with all possible velocity directions. The assumption was made that all of the ions were singly charged and the conversion of each ion-current trace to an ion-energy-distribution-function plot was accomplished using the following equation:

$$g(\varepsilon) = J(\varepsilon)/eA\tilde{\varepsilon}\sqrt{2e\varepsilon/m} \tag{1}$$

For these experiments the effective ESA acceptance area A was 3.14×10^{-2} cm^2. The energy-resolution width of the ESA $\tilde{\varepsilon}$ is defined as the kinetic energy range associated with ions that are able to pass through the entrance and exit collimator sets and the electrostatic field region in the ESA and reach the collector plate. Numerical calculation was conducted, and its value was determined to be 0.235 eV for the 2.0-mm-diam collimator apertures at the 10-eV transmission energy.[15]

The ion-energy-distribution function computed from typical raw data using Eq. (1) is shown in Fig. 5 as a thick line. As this figure suggests, it can be represented as the sum of several simple (Gaussian) distributions that add to match the overall distribution function reasonably well at all but the lowest energies (i.e., that match at energies greater than those corresponding to the anode-to-cathode potential difference V_d). By considering the Gaussian components rather than the composite function, one can track the trends in the parameters that characterize these Gaussian distributions and gain insight that is otherwise difficult to infer. These Gaussian distribution functions might not describe the measured distribution functions precisely. In fact, it is likely that other functions exist that reflect the physics

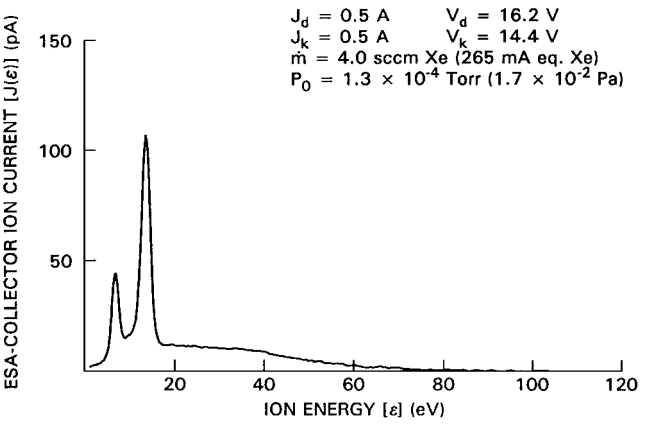

a) J_d = 0.5 A

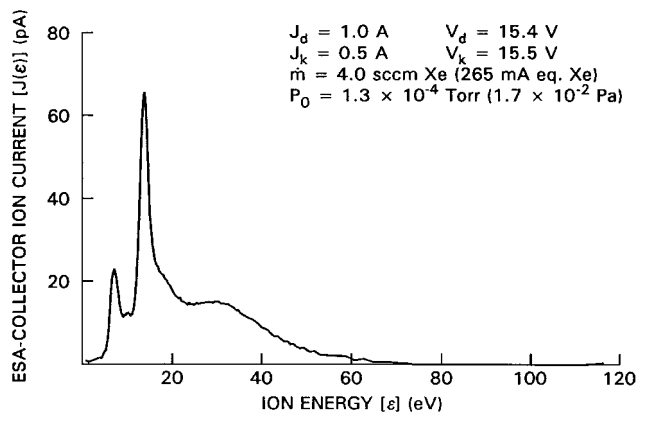

b) J_d = 1.0 A

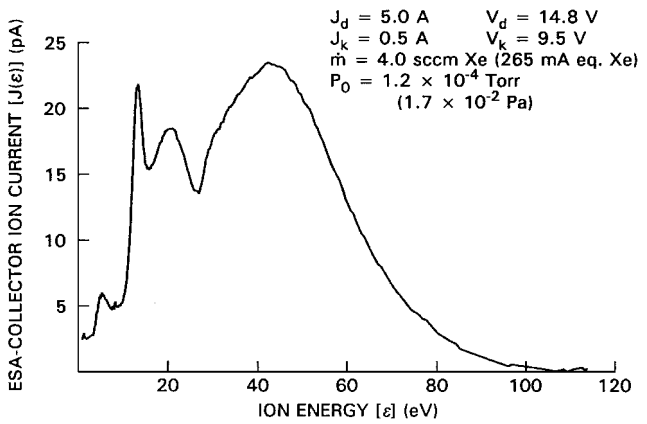

c) J_d = 5.0 A

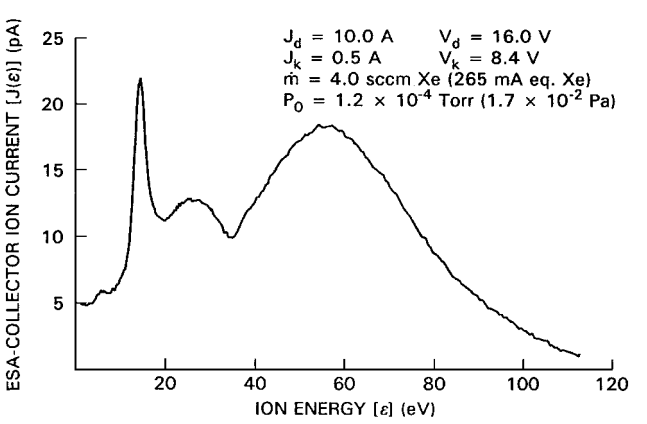

d) J_d = 10.0 A

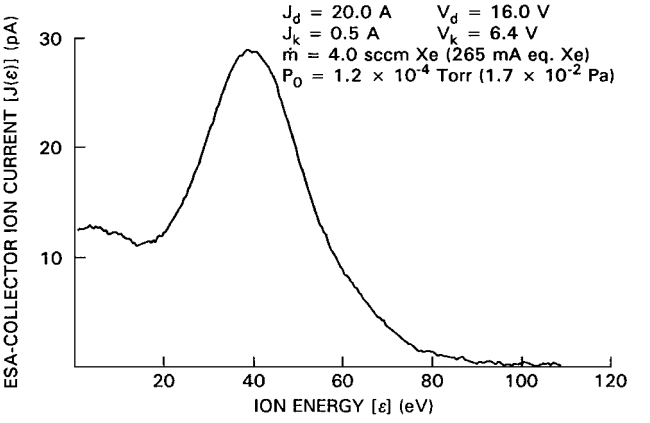

e) J_d = 20.0 A

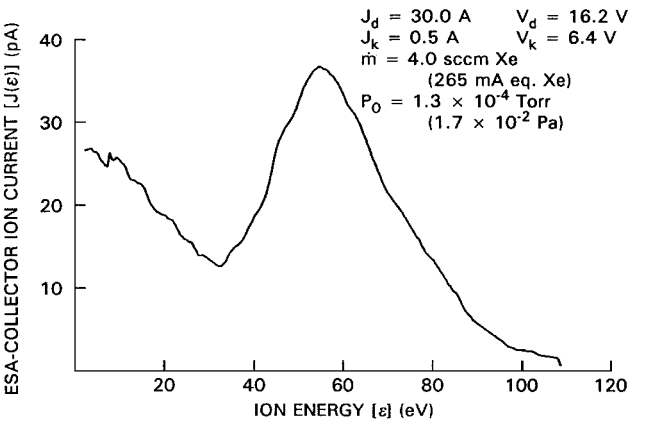

f) J_d = 30.0 A

Fig. 4 Typical traces of ESA-collector ion currents for 16-deg-chamfered-orifice cathode.

of the ion-production processes more accurately. Such functions are, however, unknown, and the Gaussians are preferred here because they are simple to use and are considered to approximate the measured distribution functions adequately. The Gaussian functions used for this purpose are given by

$$g'(\varepsilon) = \frac{n}{\sqrt{2\pi}\sigma} \exp\left[-\frac{(\varepsilon - \varepsilon_0)^2}{2\sigma^2} \right] \tag{2}$$

The parameters n, ε_0, and σ were determined by first selecting the number of Gaussian components and then obtaining values for the parameters of each Gaussian component that would minimize the mean-square difference between the overall function and the Gaussian components over a specified energy interval. This interval was selected so that each peak in the overall function would be represented by the Gaussian component with no major error when the other Gaussian components were superposed.

To quantify the degree to which the sum of Gaussian components matched the measured distribution function, two parameters were investigated. One parameter was the ratio of ion population with energies above the anode-potential energy as approximated by the sum of the Gaussian components to the measured distribution function. This parameter is given by

$$f_p = \frac{\int_{V_d}^{\infty} \sum g'(\varepsilon)\, \mathrm{d}\varepsilon}{\int_{V_d}^{\infty} g(\varepsilon)\, \mathrm{d}\varepsilon} \tag{3}$$

If the sum of the Gaussian components matches the measured overall distribution function exactly, the value of f_p is unity. Values obtained from actual data typically fell in the range 1 ± 0.1.

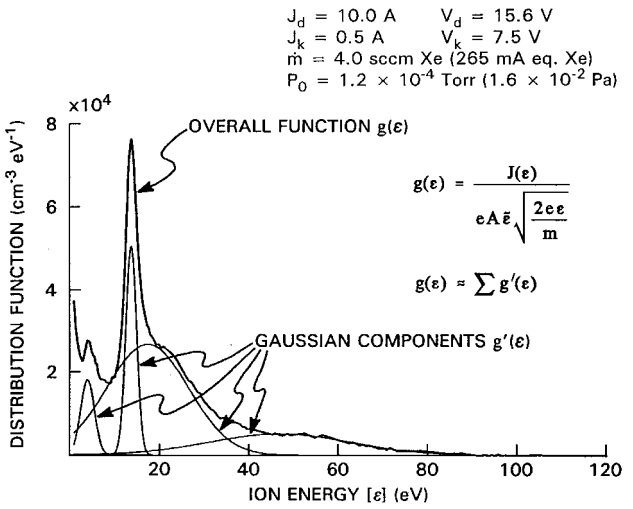

Fig. 5 Typical distribution function obtained using the ESA.

The other parameter used was designed to show the root-mean-square difference between the overall function and sum of the Gaussian components. It is given by

$$f_{\rm rms} = \frac{\sqrt{\int_{V_d}^{\infty} \left[g(\varepsilon) - \sum g'(\varepsilon)\right]^2 \mathrm{d}\varepsilon}}{\int_{V_d}^{\infty} g(\varepsilon)\,\mathrm{d}\varepsilon} \qquad (4)$$

For the case of a perfect fit, $f_{\rm rms}$ would be zero. The value of this parameter for actual data, on the other hand, typically was about 1%.

The quality of the fit was influenced primarily by the shape of the measured distribution function at energies near those associated with anode potential. When the function could not be matched by a single Gaussian component in this region (typically at discharge current $J_d \geq 20$ A), values of f_p as low as 64% and of $f_{\rm rms}$ as great as 7% were observed. Figure 6 shows comparisons of measured (thick lines) and approximate (thin lines) distribution functions under typical (Fig. 6a) and worst-fit (Fig. 6b) cases along with values of f_p and $f_{\rm rms}$. The disagreement introduced at energies near those associated with anode potential (15.4 V) is obvious in Fig. 6b.

The plots of Gaussian parameters shown in Fig. 7 facilitate an understanding of the trends involved. The data symbols and the vertical lines through each of these in Fig. 7a represent mean energies (ε_0) for the four peaks observed and the associated energy dispersions (σ), respectively. Corresponding populations are shown in Fig. 7b. Although the population is dimensionally the same as number density, it is obtained by integrating a distribution function over an energy range, and it does not represent the actual ion density. In addition, ESA-collimator acceptance angles and some possible ion-loss effects such as scattering and/or charge-exchange phenomena cause the populations shown to be small fractions of the actual ion densities in the plasma. However, these effects were considered to affect ion populations and densities in a similar way over most of the range investigated here, and a relative change in each population is, therefore, expected to reflect a corresponding density change. Three dominant groups of ions out of four shown in Fig. 5 and already described are labeled as ambient-plasma-ion components, moderate-energy-ion components, and high-energy-ion components in ascending order of mean energies. Figure 7a shows that the ambient-plasma-ion-component energies are relatively insensitive to the discharge current. This result, which is consistent with the basic trend in anode potential shown in Fig. 3, confirms the fact that ions produced in the ambient plasma fall through the anode-to-cathode potential difference when ion energies are measured relative to cathode potential. Figure 7b shows that the ion population associated with the ambient-plasma-ion component is also insensitive to changes in discharge current. At sufficiently high discharge currents (>15 A), the data of Fig. 7 indicate that ion-energy-distribution peaks corresponding to ions with energies at and below the anode-to-cathode potential

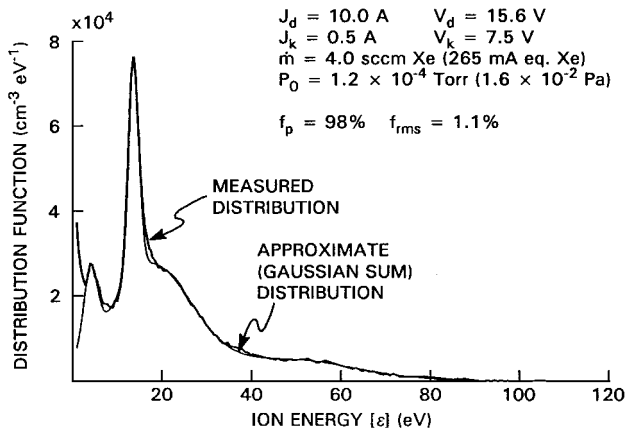

a) Typical comparison

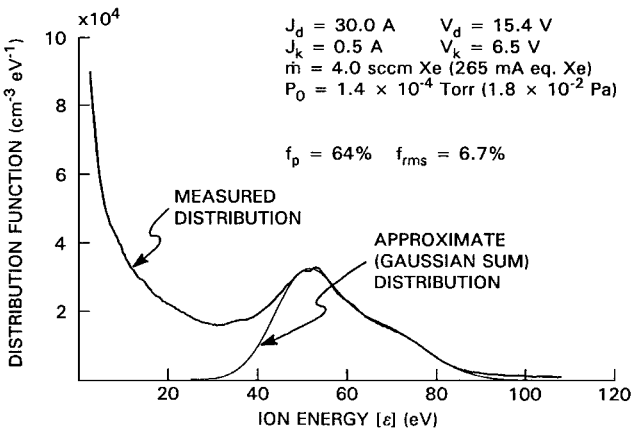

b) Worst-case comparison (measured at a high-discharge current)

Fig. 6 Distribution function goodness-of-fit comparison.

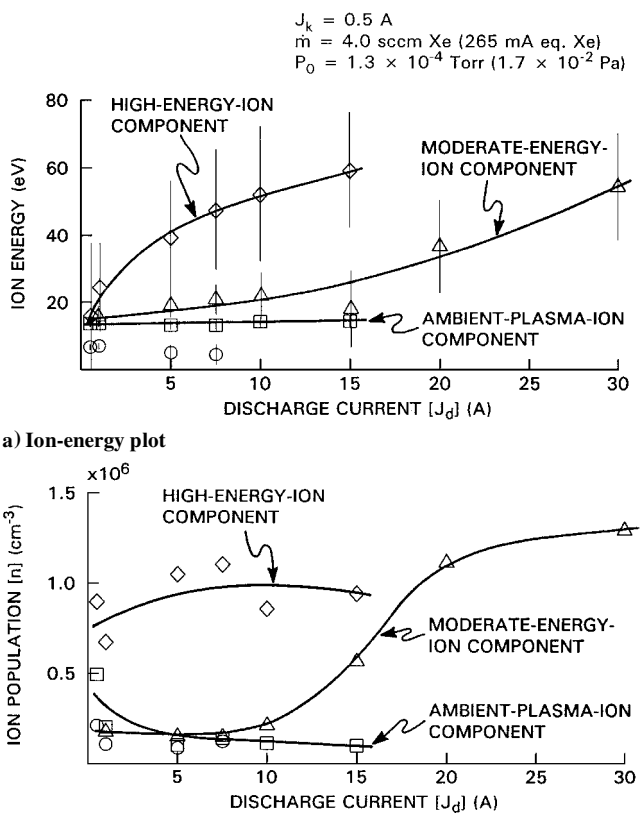

a) Ion-energy plot

b) Ion-population plot

Fig. 7 Effects of discharge current on Gaussian fit parameters for 16-deg-chamfered-orifice cathode.

difference broaden and decay to the point where they cannot be identified. On the other hand, the mean energies associated with the high- and moderate-energy components increase with discharge current. This result is consistent with the greater erosion rates on cathode-potential surfaces observed by Rawlin[16] and Brophy and Garner[17] at higher emission-current densities through cathode orifices. The populations of the high- and moderate-energy components, which are dominant over the entire range of discharge currents investigated, also grow with discharge current until the high-energy component cannot be identified ($J_d > 15$ A).

Orifice Shape Effects

In contrast to Gaussian parameter data obtained for the 16-deg-chamfered-orifice cathode, the ion energies and populations exhibit much more complex behavior for the straight-orifice cathode as shown in Fig. 8. The anode-potential transition and corresponding change in plasma appearance observed between discharge currents of 5 and 7 A (Fig. 3) are also reflected as sudden changes in the mean ion energy, energy dispersion, and ion population over a narrow current range near 7 A in Fig. 8. At discharge currents below this sudden transition, the trends are very similar to those measured with the 16-deg-chamfered orifices. As discharge current is increased above the transition region, however, all populations decrease, and mean energies increase at a more moderate rate. Figure 9 shows typical ion-energy distribution functions measured at discharge currents above and below the transition region. These data suggest that the one measured at the lower discharge current (solid line) has a relatively broad high-energy tail above the ambient-plasma-ion component. It is approximated by two Gaussian components with relatively large energy dispersion and shown as open triangles and diamonds in Fig. 8. On the other hand, the one measured at the higher discharge current (broken line) has a significantly sharper peak, and it is approximated by three Gaussian components with mean energies above the ambient-plasma-ion component (solid symbols in Fig. 8).

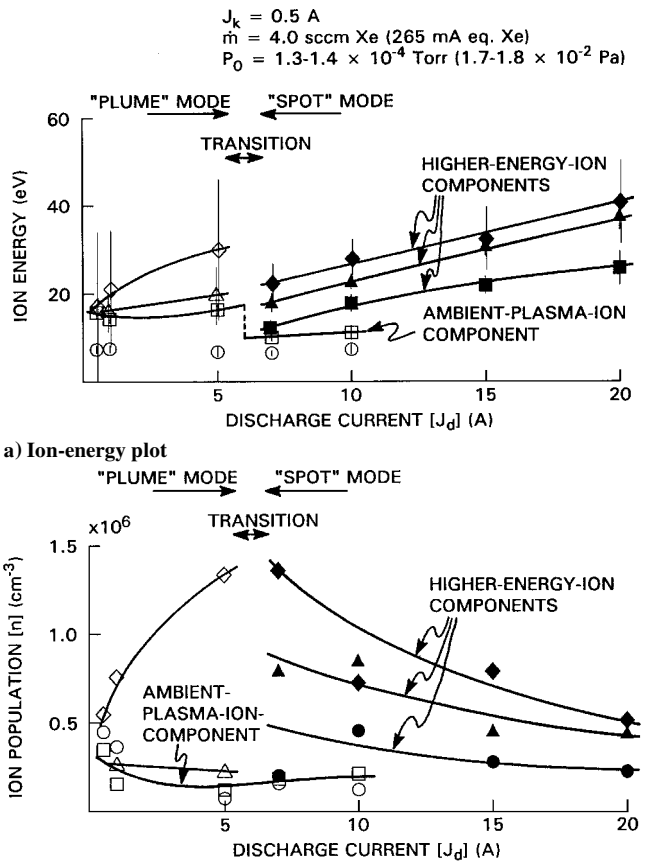

Fig. 8 Effects of discharge current on Gaussian fit parameters for straight-orifice cathode.

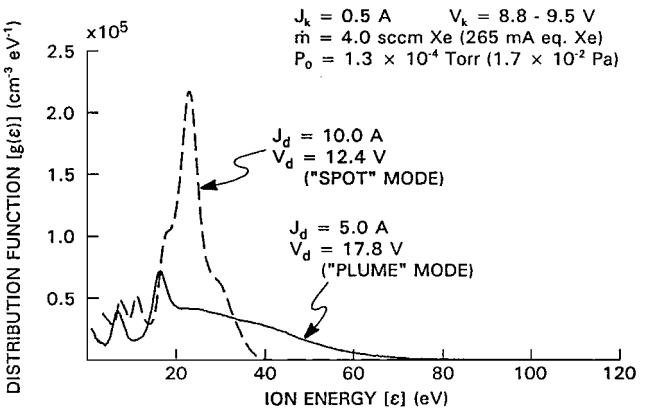

Fig. 9 Typical distribution functions for different cathode-discharge modes with straight-orifice cathode.

In contrast to the components observed at discharge currents below the transition, these are generally narrower (i.e., they have smaller dispersions) and are designated as higher-energy-ion components in Fig. 8.

During the period of testing with the straight-orifice hollow cathode at a discharge current greater than 20 A, relatively rapid erosion of the orifice plate occurred so that the distribution-function parameters associated with currents greater than 20 A are not shown in Fig. 8.

ESA/RPA Performance Comparison

The ion-energy-distribution-function data presented in this article show the same gross trends as those presented previously by Friedly and Wilbur[7] and Latham et al.,[8] but the data differ substantially in the level of detail they provide. The reasons for this are related primarily to differences in 1) fractions of the incident ions that are detected and 2) the capabilities to discriminate differences in ion energy between the instruments used in the two cases. The ESA used in this study has fine resolving power, and it samples a small fraction of the incident ions that are all moving almost in the same direction. The RPA used in the study conducted by Friedly and Wilbur could collect most of the ions incident upon it, but their energies could not be resolved without using a numerical differentiation process. Further, the instrument had poor angular resolution (i.e., it had a broad angular acceptance). Although the detailed configuration of the RPA used by Latham et al.[8] is not known, the entrance aperture on these devices is typically large and close to the ion-collection surface as it was on the one used by Friedly and Wilbur.[7] With the ESA, on the other hand, incident ions experience filtering at the entrance and exit collimator sets as well as in the electrostatic-field region, and this ensures narrow resolution bands on both angle of incidence and energy. A numerical calculation considering ion trajectories through the collimator sets and the electrostatic-field region of the ESA yields an acceptance angle of about 8 deg (Ref. 15). Even though this acceptance angle will be altered in an unknown way by the aperture ground screen, this is probably still a reasonable estimate. In contrast, it is estimated that the effective acceptance angle for the RPA used by Friedly and Wilbur[7] was more than 40 deg.

Conclusions

An ESA can be used to measure the energy distribution of ions produced in a hollow-cathode discharge. The ions emanating from high-current-hollow-cathode discharges contain 1) a low-energy component that is produced in the ambient plasma at a potential near that of the anode (the ambient-plasma-ion component) and 2) components of high-energy ions that are produced near the cathode orifice. The energies of the second group are much greater than the potential differences associated with electrode surfaces exposed to the plasma, and their magnitudes generally increase with discharge current. These results are consistent with corresponding

RPA measurements, but the ESA measurements reveal much greater detail and much more complicated energy-distribution-function structures.

The straight orifice undergoes transition to the spot mode with a drop in anode potential as the discharge current is raised above a relatively low value (< 10 A), and this is accompanied by a sudden drop in mean energies in energy-distribution function. For the 16-deg-chamfered orifice, on the other hand, a gradual change in the distribution function occurs at a higher discharge current (~15 A). All distribution functions reflect the presence of high-energy ions even though the ion populations of the components associated with the function vary with modes.

Acknowledgments

Principal financial support from Ishizaka Foundation, partial financial support from NASA Lewis Research Center under Grants NAG 3-776 and NAG 3-1206, and instrumentation support (the ESA) from Ralph Carruth at NASA Marshall Space Flight Center are gratefully acknowledged.

References

[1]Aston, G., "Ion Propulsion Technology Requirements for Planetary Mission Applications," AIAA Paper 85-2000, Sept. 1985.

[2]Aston, G., "Ferry to the Moon," *Aerospace America*, Vol. 26, No. 6, 1987, pp. 30–32.

[3]Fearn, D. G., "The Ulysses Mission: The Ion Propulsion Alternative," International Electric Propulsion Conf. Paper 91-036, Oct. 1991.

[4]Fearn, D. G., "A Mission to Pluto Using Nuclear Electric Propulsion," International Electric Propulsion Conf. Paper 93-200, Sept. 1993.

[5]Patterson, M. J., and Verhey, T. R., "5kW Xenon Ion Thruster Lifetest," AIAA Paper 90-2543, July 1990.

[6]Brophy, J. R., and Garner, C. E., "A 5,000 Hour Xenon Hollow Cathode Life Test," AIAA Paper 91-2122, June 1991.

[7]Friedly, V. J., and Wilbur, P. J., "High Current Hollow Cathode Phenomena," *Journal of Propulsion and Power*, Vol. 8, No. 3, 1992, pp. 635–643.

[8]Latham, P. M., Pearce, A. J., and Bond, R. A., "Erosion Processes in the UK-25 Ion Thruster," International Electric Propulsion Conf. Paper 91-096, Oct. 1991.

[9]Friedly, V. J., and Wilbur, P. J., "Hollow Cathode Operation at High Discharge Currents," NASA CR-185238, April 1990.

[10]Sevier, K. D., "Instrumental Methods of Electron Spectrometry and Methods of Electron Detection," *Low Energy Electron Spectrometry*, Wiley-Interscience, New York, 1972, pp. 18–32.

[11]Csiky, G. A., "Investigation of a Hollow Cathode Discharge Plasma," AIAA Paper 69-258, March 1969.

[12]Rehn, L., and Kaufman, H. R., "Correlation of Inert Gas Hollow Cathode Performance," AIAA Paper 78-707, April 1978.

[13]Fearn, D. G., Singfield, A., Wallace, N. C., Gair, S. A., and Harris, P. T., "The Operation of Ion Thruster Hollow Cathodes Using Rare Gas Propellants," AIAA Paper 90-2584, July 1990.

[14]Bohdansky, J., Roth, J., and Bay, H. L., "An Analytical Formula and Important Parameters for Low-Energy Ion Sputtering," *Journal of Applied Physics*, Vol. 51, No. 5, 1980, pp. 2861–2865.

[15]Kameyama, I., and Wilbur, P. J., "Characteristics of Ions Emitted from High-Current Hollow Cathodes," NASA CR-195372, Aug. 1994.

[16]Rawlin, V. K., "Internal Erosion Rates of a 10-kW Xenon Ion Thruster," AIAA Paper 88-2912, July 1988.

[17]Brophy, J. R., and Garner, C. E., "Tests of High Current Hollow Cathodes for Ion Engines," AIAA Paper 88-2913, July 1988.